Signal Enhancement in Magnetoelastic Ribbons through Thermal Annealing: Evaluation of Magnetic Signal Output in Different Metglas Materials

Georgios Samourgkanidis *, Dimitris Kouzoudis, Panagiotis Charalampous, Eyad Adnan

Posted Date: 20 May 2025

doi: 10.20944/preprints202505.1546.v1

Keywords: magnetoelastic materials; metglas ribbons; thermal treatment optimization; signal enhancement; sensing applications

 doi:10.20944/preprints202505.1546.v1

Article

Signal Enhancement in Magnetoelastic Ribbons through Thermal Annealing: Evaluation of Magnetic Signal Output in Different Metglas Materials

Georgios Samourgkanidis [1]*, Dimitris Kouzoudis [2], Panagiotis Charalampous [2] and Eyad Adnan [3]

[1] Department of Civil and Environmental Engineering, University of Cyprus, 1678 Nicosia, CY;
[2] Department of Chemical Engineering, University of Patras, 26504 Patras, GR;
[3] Faculty of Engineering Technology and Science, Higher Colleges of Technology, 64141 Al Ain, UAE;
* Correspondence: G.Samourgkanidis@gmail.com

Abstract: This study explores the impact of thermal annealing on the magnetic signal enhancement of three distinct Metglas ribbon materials: 2826MB3, 2605SA1, and 2714A. Each material underwent a systematic annealing process under a range of temperatures (50-500 ^{o}C) and durations (10-60 min) to evaluate the influence of thermal treatment on their magnetic signal response. The experimental setup applied a constant excitation frequency of 20 kHz, allowing for direct comparison under identical measurement conditions. Results show that while all three alloys benefit from annealing, their responses differ in magnitude, stability, and sensitivity. The 2826MB3 and 2605SA1 ribbons exhibited similar enhancement patterns, with maximum normalized voltage increases of 75.8% and approximately 70%, respectively. However, 2605SA1 displayed a more abrupt signal drop at elevated temperatures, suggesting reduced thermal stability. In contrast, 2714A reached the highest enhancement at 86.8%, but also demonstrated extreme sensitivity to over-annealing, losing its magnetic response rapidly at higher temperatures. The findings highlight the critical role of carefully optimized annealing parameters in maximizing sensor performance and offer practical guidance for the development of advanced magnetoelastic sensing systems.

Keywords: magnetoelastic materials; metglas ribbons; thermal treatment optimization; signal enhancement; sensing applications

1. Introduction

Sensors play a pivotal role in modern infrastructure, acting as the backbone of intelligent monitoring systems across a wide range of industries. They enable the continuous, real-time tracking of critical physical and chemical parameters, such as temperature, pressure, humidity, pH levels, and pollutant concentrations, which are essential for the efficient functioning and long-term sustainability of contemporary societies. In the context of urban development, sensors form the foundation of smart city technologies by regulating traffic flow, optimizing energy consumption, and managing public safety systems [1]. Environmental monitoring applications rely heavily on sensors to assess air quality by detecting gases like CO_x, NO_x, and particulate matter, as well as to track water quality parameters such as turbidity, pH, and the presence of harmful contaminants [2,3]. Moreover, advanced sensor networks are employed in waste water and sewer systems to detect anomalies, prevent blockages, and reduce pollution, thereby contributing to ecological protection and resource management [4]. In agriculture, sensor technologies are integrated into precision farming systems to monitor soil moisture, nutrient content, and crop health, ultimately leading to improved yield, reduced resource consumption, and more sustainable food production practices [5,6].

Among the diverse range of materials utilized in sensor technologies, magnetoelastic alloys hold a particularly valuable position due to their unique combination of magneto-mechanical coupling, affordability, and functional robustness [7,8]. These materials exhibit the distinct ability to undergo

 doi:10.20944/preprints202505.1546.v1

elastic deformation in the presence of an external magnetic field, and conversely, to develop magnetization when subjected to mechanical strain [9,10]. This bidirectional interaction underpins their functionality in various applications, most notably in anti-theft security systems, where they are commonly embedded as thin tags in retail products. Magnetoelastic alloys are typically composed of amorphous metallic structures, more widely known as metallic glasses or Metglas, which are formed by rapidly cooling molten metal to prevent crystallization [11–13]. Their non-crystalline nature imparts high electrical resistivity and significantly reduces eddy current losses, making them well-suited for use in high-efficiency transformers [14–16] and low-loss magnetic sensors [17,18]. Additionally, their soft magnetic properties, characterized by a near-linear relationship between the applied magnetic field and the resulting magnetization [19–21], enable predictable and sensitive magnetic responses. This makes them particularly advantageous for use in dynamic sensing environments where signal accuracy and responsiveness are critical. In practical applications, magnetoelastic ribbons have been effectively utilized in systems such as gas sensors [22–24], bio-sensors [25,26], and vibration detectors [27–31]. These devices rely on the material's sensitivity to mechanical or environmental changes, enabling them to function as highly responsive transducers. The operating principle of magnetoelastic sensors is analogous to that of piezoelectric crystals in the magnetic domain, where fine-tuning the magnetic response is essential for accurately capturing even subtle magnetic field variations.

In this study, three different Metglas alloys, 2826MB3, 2605SA1, and 2714A, were selected based on their distinct magnetic and structural properties that make them suitable for sensing applications. Metglas 2826MB3 is an iron-nickel-based alloy offering medium saturation induction, low magnetostriction, and high corrosion resistance. It is commonly used in field sensors [18], magnetomechanical systems [32,33], and high-frequency magnetic cores [34], with the flexibility to be annealed for high permeability or a tailored BH loop shape, making it highly adaptable to different magnetic environments. Metglas 2605SA1, an iron-based alloy, is engineered for applications requiring extremely low core losses and high permeability. Its excellent performance in distribution transformers [35], current sensors [36], and motors [37] is attributed to its ability to minimize energy dissipation, particularly at both low and high frequencies. Lastly, Metglas 2714A is a cobalt-based alloy notable for its near-zero magnetostriction and ultrahigh magnetic permeability, making it ideal for ultra-sensitive applications such as magnetic amplifiers [38], shielding [39], and precision sensors [40]. It combines extremely low core loss with a high squareness ratio and can be annealed for a linear BH response.

Several prior studies have investigated the effects of annealing on various Metglas alloys, revealing how thermal treatment can significantly alter their magnetic properties. Cadogan et. al.[41] investigated the embrittlement behavior of metglas 2605S2 , identifying a ductile-to-brittle transition near 310 ^{o}C, marked by a five-fold reduction in fracture toughness. Using Mössbauer spectroscopy, they observed increased magnetic texturing in both the bulk and surface of the ribbons upon annealing, linked to stress relaxation. Despite these changes, no significant structural modifications were detected via X-ray diffraction, emphasizing the subtle yet critical effects of thermal treatment on the alloy's mechanical and magnetic properties. Teng et al. [42] found that annealing FeBSiC Metglas at 360 ^{o}C for 10 minutes produces a mixed amorphous crystalline phase, leading to improved piezomagnetic properties and reduced magnetic loss. This optimized structure enhanced ME coupling in composite sensors, increasing Q by up to 37.5% and lowering the equivalent magnetic noise, thereby significantly boosting low-frequency detection sensitivity. Lee et al. [43] reported that annealing the Co-based amorphous alloy $Co_{67}Fe_3Cr_3B_{12}Si_{15}$ at 350 ^{o} for 1 hour significantly enhanced its magnetic properties, making it suitable for use in low-noise flux-gate magnetometers. The optimized ribbons demonstrated a noise level of 2.4 nT at 1 Hz and 0.1 nT peak-to-peak in a 1 Hz bandwidth. These findings highlight the alloy's potential for high-frequency sensing applications and its suitability as a long-term, stable core material in precision magnetic devices. Sun et. al. [44] compared the magnetomechanical performance of Fe-based amorphous ribbons, Vitrovac 7600 (FeCoSiB) and Metglas 2605SA1 (FeSiB), under various annealing conditions. They found that Metglas 2605SA1 significantly outperformed Vitrovac, achieving a maximum coupling factor of 73% and a magnetomechanical efficiency factor (k^2Q) as high

 doi:10.20944/preprints202505.1546.v1

as 16 after partial crystallization at elevated annealing temperatures. In contrast, Vitrovac exhibited a peak coupling factor of 23% and lower overall efficiency. These results confirm that appropriately annealed Metglas 2605SA1 ribbons offer superior power conversion efficiency, making them better suited for applications such as magnetostrictive actuators and acoustically driven antennas. Wang et al. [45] developed a novel multi-component Fe-based amorphous alloy (FeMnCuMoCPSiB) featuring a surface crystallization layer composed of ultra-fine nano α-Fe grains. This engineered structure resulted in superior soft magnetic properties (SMPs), including a high saturation magnetic induction (B_s) of 1.67 T, low coercivity (H_c) of 1.6 A/m, and high initial permeability (μ_i) of 0.00093 at 1 kHz, significantly outperforming commercial Metglas 2605. Their findings underscore the role of nanoscale surface precipitation in enhancing, rather than degrading, magnetic performance, and present an effective pathway for advancing soft magnetic material design for applications in electronics and energy systems. Palneedi et al. [46] demonstrated a novel fabrication method for magnetoelectric (ME) heterostructured films by depositing PZT thick films onto Metglas substrates using aerosol deposition, followed by rapid annealing via intense pulsed light (IPL). This approach enabled effective crystallization of the piezoelectric phase without thermally degrading the Metglas, overcoming a major limitation in traditional high-temperature processing. Through optimization of IPL pulse duration, particularly at 0.75 ms, they achieved significantly enhanced ME coupling, reaching around 20 $Vcm^{-1}Oe^{-1}$, which is an order of magnitude higher than previously reported values. Their work highlights the potential of IPL-treated PZT/Metglas composites for high-performance, miniaturized ME devices such as sensors, energy harvesters, and RF components.

Building upon our previous work [47], which focused exclusively on the annealing behavior of metglas 2826MB3 at a fixed excitation frequency of 1 kHz, the present study extends the investigation in two significant directions. First, it broadens the scope by comparing the thermal response of three distinct metglas alloys, 2826MB3, 2605SA1, and 2714A, under identical annealing conditions, allowing for a direct evaluation of compositional effects on magnetoelastic signal enhancement. Second, this work advances the frequency domain of analysis by shifting to a higher excitation frequency of 20 kHz, providing new insights into the performance of these materials in more demanding sensing environments. Through this comparative and frequency-expanded approach, the study aims to offer a more comprehensive understanding of how thermal treatment influences magnetic signal output across different metglas compositions.

2. Materials and Methods

In this study, three different magnetoelastic materials were selected for investigation: Metglas 2826MB3, Metglas 2605SA1, and Metglas 2714A. Figure 1 presents the hysteresis loops for all three materials, while Table 1 summarizes key general properties as provided by the manufacturer. Among the three metglas types, 2605SA1 exhibits the highest value of saturation magnetic induction, whereas 2714A has the lowest. Regarding crystallization temperature, 2714A shows the highest value, reaching up to 550 ^{o}C, also based on manufacturer data. This temperature is particularly significant, as it marks the threshold at which the alloy transitions from its amorphous state, leading to immediate and pronounced changes in its magnetic properties, an effect that will be discussed further in the results section.

 doi:10.20944/preprints202505.1546.v1

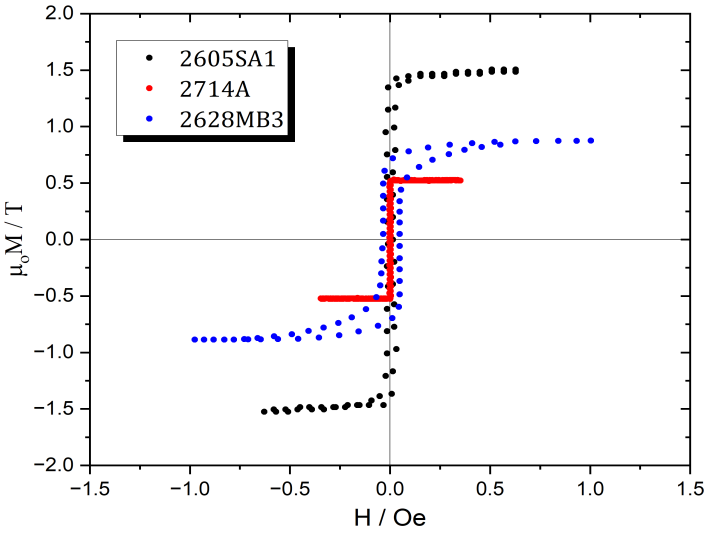

(a)

Figure 1. Magnetic hysteresis curves for all tested metglas materials.

Table 1. Material properties of the metglas ribbons, based on data from the Metglas Inc. website.

Properties	2628MB3	2605SA1	2714A
Base material	Fe-Ni	Fe	Co
Density (g / cm^3)	7.90	7.18	7.59
Saturation Induction (T)	0.88	1.56	0.57
Saturation Magnetostriction (ppm)	12	27	< 0.5
Curie Temperature (^{o}C)	353	395	225
Crystallization Temperature (^{o}C)	410	510	550

Each material was obtained in ribbon form, with a uniform width of 1/4 inch and a thickness of 30 μm. The ribbons were cut into equal lengths to ensure consistency during experimentation. For each material type, one ribbon was retained in its unannealed condition to serve as a control specimen. The remaining ribbons underwent thermal annealing under various conditions to evaluate the effect of heat treatment on magnetic signal response. The annealing temperature was varied from 50 ^{o}C to 500 ^{o}C in increments of 50 ^{o}C, and the annealing time ranged from 10 to 60 minutes in 10 minute intervals. This matrix of temperature and time resulted in 60 unique annealing conditions per material type. Consequently, 60 ribbons were prepared and thermally treated for each metglas alloy, leading to a total of 180 ribbon specimens analyzed in the study (Figures 2(a)–2(c)).

 doi:10.20944/preprints202505.1546.v1

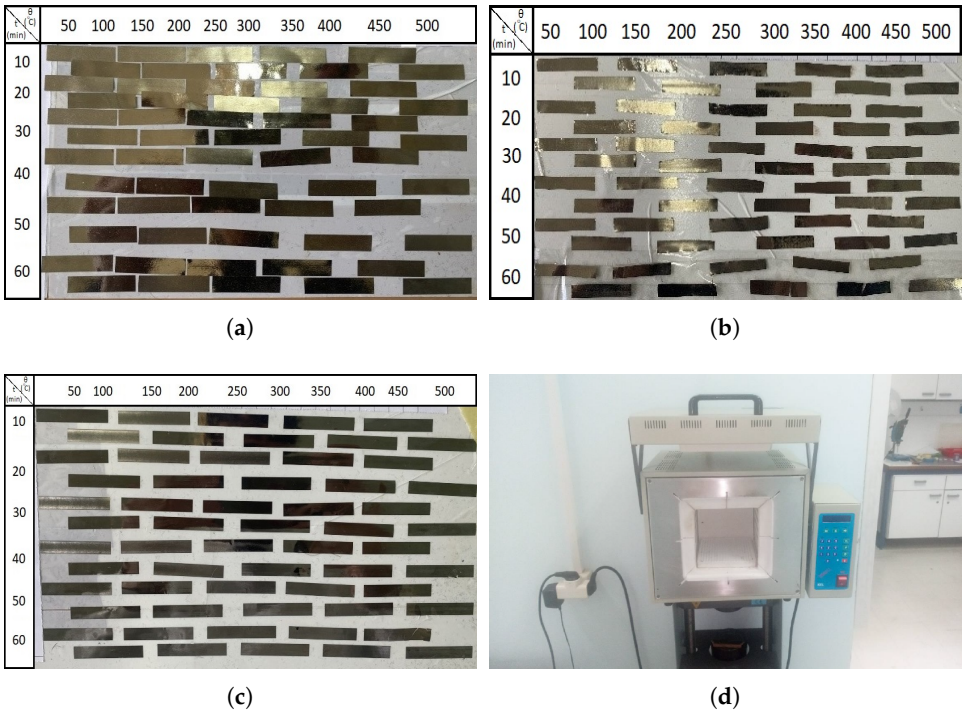

Figure 2. All ribbon specimens prepared for thermal annealing for each metglas material: (a) Metglas 2826MB3, (b) Metglas 2605SA1, and (c) Metglas 2714A. (d) The furnace used for the annealing process.

The annealing process was conducted identically for all three metglas materials. For each target temperature the furnace (Figure 2(**d**)) was first allowed to stabilize at the set temperature. Then, a group of six ribbons from a given metglas type was placed into the furnace, with each ribbon designated for a specific annealing time between 10 and 60 minutes, increasing in 10-minute steps. After each time interval elapsed, the corresponding ribbon was individually removed and allowed to cool naturally in ambient conditions. This procedure was repeated for all temperature levels and for each material type.

The experimental setup used to evaluate the magnetoelastic signal response of each ribbon specimen is illustrated in Figure 3. The system consists of two Helmholtz coil pairs: the inner coils are connected to a DC power supply that generates a static bias magnetic field, while the outer coils are driven by a function generator to produce a low-amplitude alternating magnetic field. Positioned at the center of these coils is a detection coil, into which the magnetoelastic ribbon is inserted. This detection coil captures the time-varying magnetic signal induced by the ribbon's ferromagnetic behavior. The output signal is then amplified using a pre-amplifier and its amplitude measured with a digital voltmeter. The test procedure is as follows: a ribbon is placed inside the detection coil, and an AC magnetic field is applied in the form of a sinusoidal excitation, defined as $\Delta H = H_0\cos(2\pi ft)$ with a fixed excitation frequency of 20 kHz. Simultaneously, a constant DC magnetic field H_{DC} is applied to bias the ribbon to its optimal working point. This biasing condition is standard in magnetoelastic sensing applications, as it maximizes the linearity of the sensor's input-output response and improves signal clarity. As a result of its ferromagnetic nature, the ribbon develops a time-varying magnetization $\Delta M = M_0\cos(2\pi ft)$, which induces a changing magnetic flux in its surroundings. According to Faraday's law of electromagnetic induction, this changing flux generates an AC voltage across the detection coil $V = V_0\sin(2\pi ft)$. This voltage signal, which is amplified and read by the voltmeter, is directly related to the rate of change of magnetization. Given the relationship $\chi = \Delta M/\Delta H$ and since both f and H_0 are held constant throughout the experiments, any observed increase in voltage amplitude V_0 can be attributed to an increase in magnetic susceptibility χ of the ribbon. This method was uniformly applied across all three Metglas materials under study, allowing for a direct comparison of their magnetoelastic signal responses under identical excitation and biasing conditions.

 doi:10.20944/preprints202505.1546.v1

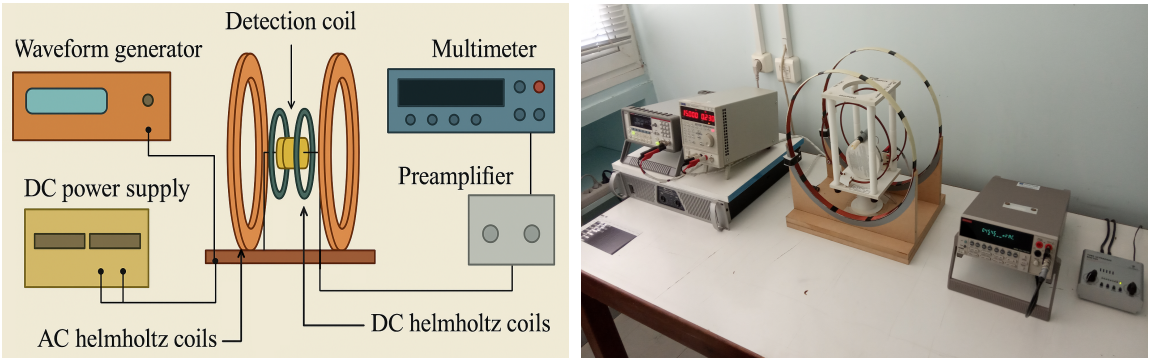

(**a**) (**b**)

Figure 3. Experimental setup used for magnetoelastic signal measurement: (a) Schematic diagram and (b) Actual setup.

The thermal annealing process serves to relieve internal stresses within the material, which are a primary contributor to elevated magnetic anisotropy energy and, consequently, a high anisotropy field [48]. By reducing this internal stress, the anisotropy field is lowered, resulting in an increase in magnetic susceptibility. In this study, the method involves comparing the measured voltage signals of each ribbon before and after annealing to identify the optimal annealing conditions that maximize magnetic response.

At this point, we would also like to explain why 20 kHz was chosen as the fixed excitation frequency for this study. This decision is based on insights from two prior studies conducted by our research group. In the first study [33], metglas 2826MB3 demonstrated a broad and stable frequency response across the range of 300 Hz to 50 kHz, confirming its reliable performance throughout that spectrum. In a follow-up work [47], we specifically investigated the annealing behavior of 2826MB3 at a fixed frequency of 1 kHz, revealing how thermal treatment influenced its signal response. Building upon these findings, we selected 20 kHz in the present study to examine whether such behavior remains consistent, or potentially changes, when different metglas ribbons are tested at a higher operating frequency within the known stable region.

3. Results and Discussion

The sensing procedure was implemented as follows: Initially, with the detection coil empty (Figure 3), the amplifier was calibrated so that the voltmeter displayed a baseline voltage of 1 mV, which served as the system's reference signal. After calibration, an unannealed ribbon was placed inside the detection coil, and the resulting output voltage was recorded as V_a. Following the annealing process, each treated ribbon was similarly inserted into the coil, and the new voltage output, V_b, was measured. The difference, defined as $\Delta V = V_b - V_a$ was used to assess the effect of annealing on the ribbon's signal response. All measurements were conducted under identical experimental conditions, with a DC bias field applied at its optimized level to enhance magnetic response and improve signal detection sensitivity.

3.1. Metglas 2826MB3

Figure 4 presents a 2D color-map illustrating the normalized ΔV (%) response of the 2826MB3 ribbons as a function of annealing temperature (vertical axis) and time (horizontal axis). The color scale to the right indicates the degree of signal enhancement, with values ranging from approximately 31% to 76%. Compared to our earlier study at 1 kHz [47], where a similar mapping was performed, the overall shape of the response remains consistent at 20 kHz. However, a noticeable difference lies in the magnitude of the enhancement: the previous results showed a peak near 100%, while the current measurements reach up to around 76%.

 doi:10.20944/preprints202505.1546.v1

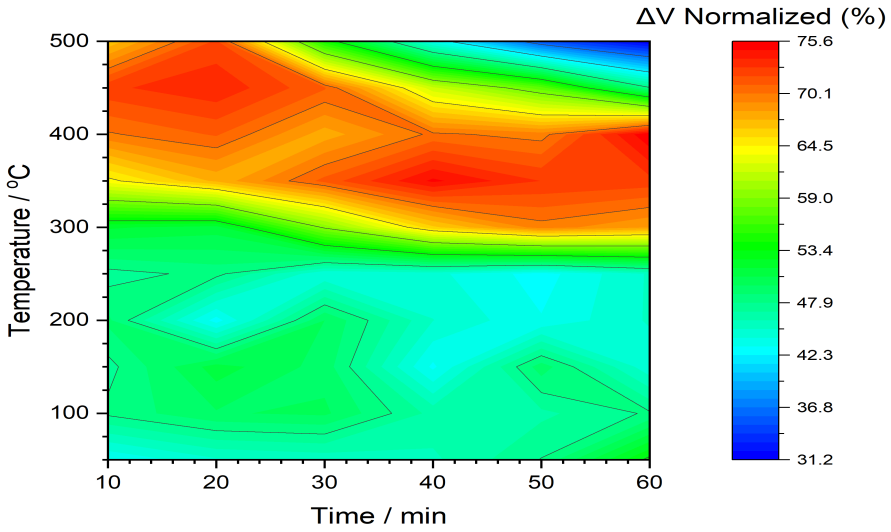

Figure 4. 2D color-map of normalized ΔV (%) for 2826MB3 ribbons as a function of annealing temperature and time.

According to Table 1, the Curie temperature of the alloy is approximately 353 ^{o}C and the onset of crystallization begins at around 410 ^{o}C. Notably, a significant rise in signal begins near 300 ^{o}C, transitioning from mid-range values (teal-green, around 45%) to much higher values (around 75%, red). The red contours, representing peak enhancement, spread over a wide time window, gradually shifting to lower temperatures as annealing time increases. This suggests a temperature-time trade-off to achieve optimal signal amplification. At the upper-right region of the plot, a shift to dark blue (around 31%) indicates a drop in signal strength at prolonged annealing times and high temperatures (470 ^{o}C - 500 ^{o}C). This decline likely corresponds to structural changes in the material, possibly due to ongoing crystallization as the alloy is already 60 ^{o}C to 90 ^{o}C above its critical transformation temperature.

Figure 5 displays the 3D surface representation of ΔV, offering a clearer view of the signal enhancement region. The elevated area, corresponding to the highest normalized values, spans a range of approximately 70-75%. Surface fitting analysis identifies two distinct peak points: one at 457 ^{o}C and 22 min, and another at 356 ^{o}C and 41 min, both reaching a maximum value of 75.8%. Conversely, the minimum response of 32.3% is observed at the far end of the plot, where both temperature and time are at their highest.

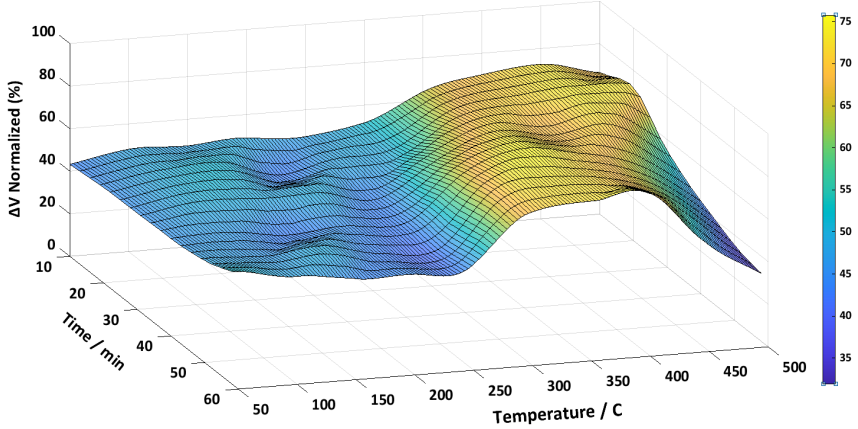

Figure 5. 3D surface plot of normalized ΔV (%) for 2826MB3 ribbons as a function of annealing temperature and time.

 doi:10.20944/preprints202505.1546.v1

3.2. Metglas 2605SA1

For the Metglas 2605SA1 alloy, the overall behavior closely resembles that of 2826MB3. As shown in the corresponding colormap (Figure 6), an optimal annealing region is evident at elevated temperatures and across a range of times, similar to the previous case. Additionally, a steep drop in signal is observed at the upper-right section of the map, indicating degradation at prolonged annealing times and high temperatures. However, this decline begins earlier than in 2826MB3, as the blue region extends toward shorter annealing durations. While the maximum signal enhancement in the red region remains comparable, around 70%, a key difference lies in the severe drop in performance within the blue region, where the normalized ΔV falls to nearly 2%. This suggests a substantial loss of magnetic properties under certain conditions. According to Table 1, the Curie and crystallization temperatures for this alloy are 395 ^{o}C and 510 ^{o}C, respectively, both higher than those of 2826MB3. This explains the sharp decline in magnetic performance observed near 500 ^{o}C, as seen in the colormap. In contrast, for 2826MB3, despite its lower crystallization temperature of 410 ^{o}C, the material maintains a strong signal response even at elevated temperatures and short annealing times, suggesting lower crystallization rate compared to 2605SA1. Another notable feature is the presence of orange to light red zones at lower temperatures (below 200 ^{o}C), indicating a signal enhancement slightly exceeding 50%.

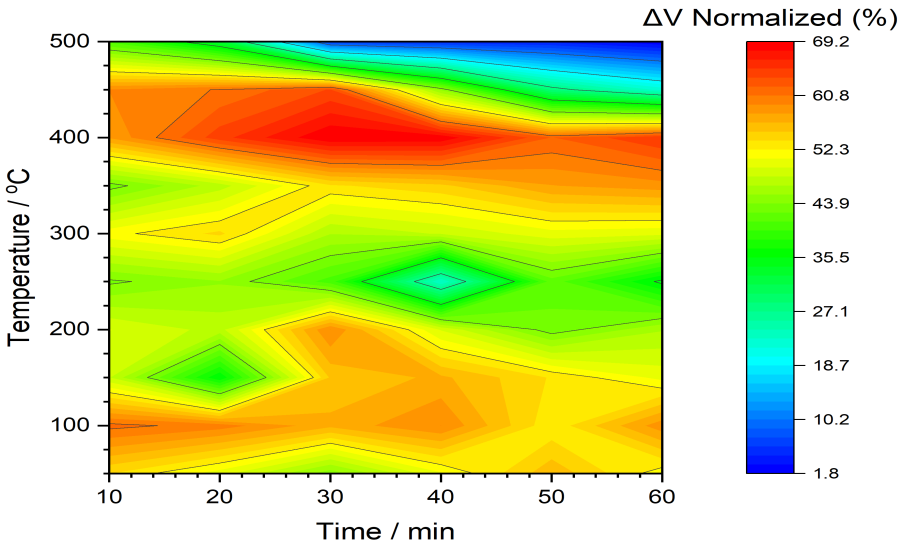

Figure 6. 2D color-map of normalized ΔV (%) for 2605SA1 ribbons as a function of annealing temperature and time.

The 3D surface representation of ΔV for this alloy exhibits a more uneven profile (Figure 7), with pronounced peaks and valleys across the temperature and time axes. The decline in signal at higher temperatures is significantly steeper compared to the previous alloy, with the fitted minimum value dropping to just 1.6% at 500 ^{o}C and 60 min. In contrast, a single distinct peak is observed at 412 ^{o}C and 31 min, marking the optimal annealing conditions for this material.

 doi:10.20944/preprints202505.1546.v1

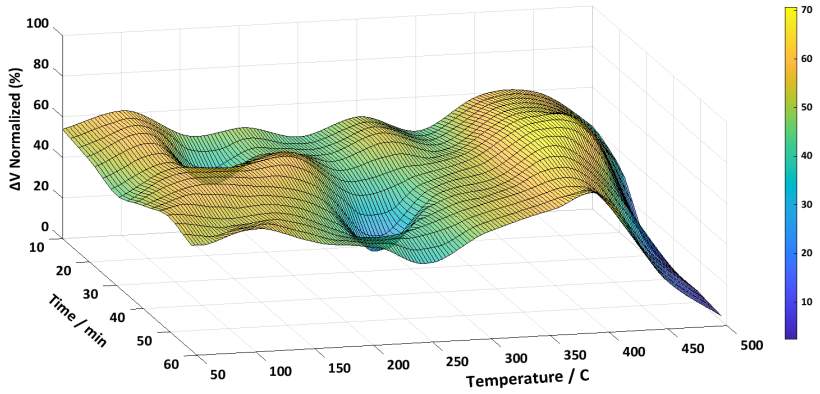

Figure 7. 3D surface plot of normalized ΔV (%) for 2605SA1 ribbons as a function of annealing temperature and time.

3.3. Metglas 2714A

This ribbon displays behavior markedly different from the other alloys. As shown in its colormap, the annealing process maintains relatively stable signal enhancement over a broad range, with the green region averaging around 52%. The area of highest enhancement (red) appears in the upper-left portion of the map, while the blue zone, indicating signal suppression, is widespread across much of the high-temperature range (>400 ^{o}C). According to Table 1, this alloy's crystallization temperature is 550 ^{o}C. The extensive presence of the blue region, combined with low signal values similar to those observed in 2605SA1, suggests that temperatures exceeding approximately 72% of the crystallization point significantly degrade the material's performance, highlighting its sensitivity to thermal treatment.

The 3D surface plot of ΔV for this alloy clearly reveals a temperature boundary, with a sharp decline in signal occurring beyond 400 ^{o}C. The peak ΔV value, which is the highest among all tested ribbons at 86.8%, is observed near 439 ^{o}C and 10 minutes. However, surface fitting analysis refines this to a maximum at approximately 9 min and 442 ^{o}C. This further underscores the alloy's sensitivity to thermal treatment, as even slight variations in time and temperature significantly impact performance.

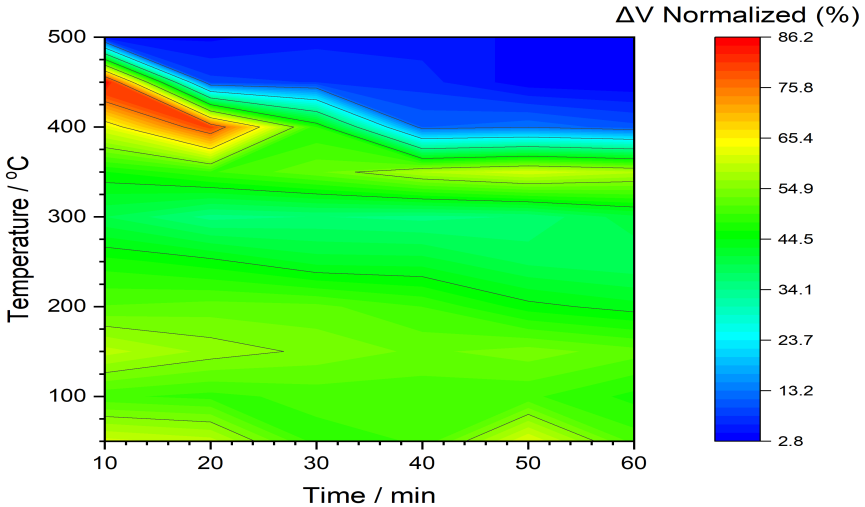

Figure 8. 2D color-map of normalized ΔV (%) for 2714A ribbons as a function of annealing temperature and time.

 doi:10.20944/preprints202505.1546.v1

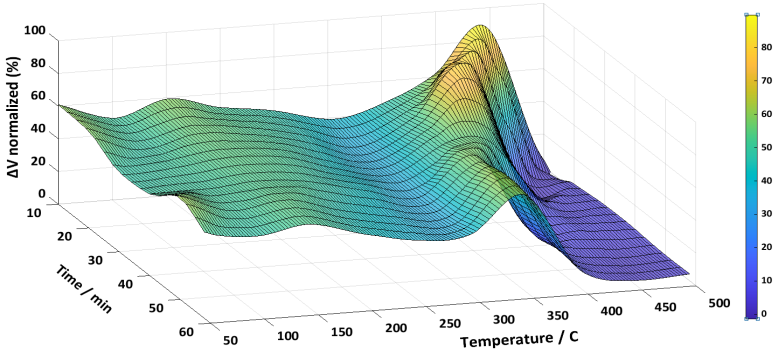

Figure 9. 3D surface plot of normalized ΔV (%) for 2714A ribbons as a function of annealing temperature and time.

3.4. Reported benefits of thermal annealing in literature

Table 2 compiles reported improvements in magnetoelastic and related properties achieved through thermal annealing, drawing from both prior literature and the present study. The data illustrate a consistent trend: carefully optimized annealing protocols lead to significant enhancements in performance metrics such as magnetic permeability, coupling efficiency, noise suppression, magnetic signal output etc. [41] reported a marked improvement in in-plane magnetic texture of Fe-based metglas 2605S2 after annealing at 360 ^{o}C for 5 minutes, where the bulk intensity ratio increased from 2.2 to 2.8, attributed to stress-relief and structural relaxation effects. In [42], annealing Mn-PMNT/FeBSiC composites at 360 ^{o}C led to a 36.8% increase in the piezomagnetic coefficient, directly enhancing ME sensitivity at low frequencies. [43] observed significant noise reduction in flux-gate magnetometers by annealing $Co_{67}Fe_3Cr_3B_{12}Si_{15}$ at 350 ^{o}C for 60 minutes, achieving a noise level of 2.4 nT at 1 Hz, twice as quiet as sensors using untreated metglas 2714A cores. [44] compared two amorphous alloys and found that annealing metglas 2605SA1 at 440 ^{o}C for 20 minutes yielded a coupling factor of 73%, greatly surpassing Vitrovac 7600, which peaked at 23% at 390 ^{o}C for 20 minutes. In [45], a multi-component Fe-based alloy exhibited not only a 136.8% increase in initial permeability (from 0.0057 to 0.00135) after annealing at 523 ^{o}C, but also a 50% reduction in core losses, emphasizing that thermal treatment can simultaneously optimize energy efficiency and magnetic performance. Meanwhile, [46] achieved a record-breaking ME coupling of 20 $Vcm^{-1}Oe^{-1}$ in PZT/Metglas composites using intense pulsed light (IPL) annealing, showcasing a novel method that enhances piezoelectric phase crystallization without compromising the magnetic substrate. In the present study, significant signal amplification was achieved through conventional thermal annealing: Metglas 2826MB3 showed a peak normalized signal gain of 75.8%, Metglas 2605SA1 reached 70%, and Metglas 2714A achieved the highest increase at 86.8%. These findings further affirm the critical role of carefully tuned annealing parameters in optimizing the performance of magnetoelastic and magnetoelectric systems across diverse applications.

 doi:10.20944/preprints202505.1546.v1

Table 2. Literature and current work (CW) results are presented, where OAS refers to the optimal annealing settings used in each study.

Ref.	Alloy	OAS (^{o}C-min)	Property	Improvement
[41]	$Fe_{78}Si_9B_{13}$ (Metglas 2605S2)	360 - 5	In-plane magnetic texture	27.2 %
[42]	Mn-PMNT/FeBSiC	360 - 5	Piezomagnetic coefficient	36.8 %
[43]	$Co_{67}Fe_3Cr_3B_{12}Si_{15}$	350 - 60	Noise level	108.3 %
[44]	FeCoSiB (Vitrovac 7600)	390 - 20	Coupling factor	23 %
	FeSiB (Metglas 2605SA1)	440 - 20	//	73 %
[45]	$Fe_{74.89}Cr_{3.04}Ni_{1.23}Co_{0.11}Mn_{0.47}Cu_{0.02}Mo_{0.01}C_{0.11}P_{0.12}Si_9B_{11}$	523 - 10	Magnetic permeability	136.8 %
	$Fe_{78.32}Mn_{0.49}Cu_{0.02}Mo_{0.01}C_{0.12}P_{0.13}Si_{9.41}B_{11.5}$	521 - 10	Core losses	50 %
[46]	$Pb(Zr,Ti)O_3$/FeSiB (PZT/Metglas 2605SA1)	300 - 2	Magnetoelectric coupling	≈1000 %
CW	$Fe_{37}Ni_{42}Mo_4B_{17}$ (Metglas 2826MB3)	457 - 22	Magnetic signal	75.8 %
	FeSiB (Metglas 2605SA1)	412 - 31	//	70 %
	$Co_{66}Fe_4Ni_1B_{14}Si_{15}$ (Metglas 2714A)	442 - 9	//	86.8 %

4. Conclusions

The results of this study demonstrate that thermal annealing significantly influences the magnetoelastic signal response of Metglas ribbon materials, with each alloy exhibiting distinct behavior under identical processing and measurement conditions. The 2826MB3 alloy showed stable signal enhancement with a broad optimal annealing range and a peak normalized ΔV of 75.8%, confirming its suitability for thermal treatment. The 2605SA1 ribbons presented a similar trend in maximum enhancement (70%) but exhibited sharper degradation at elevated temperatures, indicating greater thermal sensitivity. In contrast, the 2714A alloy displayed a unique profile, achieving the highest recorded enhancement at 86.8%, yet also experiencing a rapid decline in performance at temperatures exceeding 72% of its crystallization point. This highlights the alloy's strong responsiveness but also its vulnerability to over-annealing. These findings underline the importance of the annealing conditions, specifically temperature and duration, to the specific thermal characteristics of each alloy. By identifying the optimal processing parameters, this work contributes to the advancement of magnetoelastic materials for sensing applications, offering a practical framework for enhancing signal output through controlled thermal treatment.

Author Contributions: Conceptualization, G.S., D.K. and P.C.; methodology, G.S., D.K. and P.C.; software, G.S.; validation G.S. and P.C.; formal analysis, G.S. and D.K.; investigation, G.S. and P.C.; resources, G.S. and D.K.; data curation, G.S. and E.A.; writing—original draft preparation, G.S. and E.A.; writing—review and editing, G.S.; visualization, G.S.; supervision, G.S. and D.K.; project administration, G.S. and D.K. All authors have read and agreed to the published version of the manuscript.

Funding: This research received no external funding.

Data Availability Statement: Data available on request from the authors.

Conflicts of Interest: The authors declare no conflict of interest.

References

1. Goumiri, S.; Yahiaoui, S.; Djahel, S. Smart Mobility in Smart Cities: Emerging challenges, recent advances and future directions. *Journal of Intelligent Transportation Systems* **2025**, *29*, 81–117.
2. Kang, Y.; Aye, L.; Ngo, T.D.; Zhou, J. Performance evaluation of low-cost air quality sensors: A review. *Science of The Total Environment* **2022**, *818*, 151769.
3. Zainurin, S.N.; Wan Ismail, W.Z.; Mahamud, S.N.I.; Ismail, I.; Jamaludin, J.; Ariffin, K.N.Z.; Wan Ahmad Kamil, W.M. Advancements in monitoring water quality based on various sensing methods: a systematic review. *International Journal of Environmental Research and Public Health* **2022**, *19*, 14080.
4. Alshami, A.; Ali, E.; Elsayed, M.; Eltoukhy, A.E.; Zayed, T. IoT Innovations in Sustainable Water and Wastewater Management and Water Quality Monitoring: A Comprehensive Review of Advancements, Implications, and Future Directions. *IEEE Access* **2024**.

 doi:10.20944/preprints202505.1546.v1

5. Sishodia, R.P.; Ray, R.L.; Singh, S.K. Applications of remote sensing in precision agriculture: A review. *Remote sensing* **2020**, *12*, 3136.
6. Getahun, S.; Kefale, H.; Gelaye, Y. Application of precision agriculture technologies for sustainable crop production and environmental sustainability: A systematic review. *The Scientific World Journal* **2024**, *2024*, 2126734.
7. Xu, J.; Tat, T.; Zhao, X.; Zhou, Y.; Ngo, D.; Xiao, X.; Chen, J. A programmable magnetoelastic sensor array for self-powered human–machine interface. *Applied Physics Reviews* **2022**, *9*.
8. Shekhar, S.; Karipott, S.S.; Guldberg, R.E.; Ong, K.G. Magnetoelastic sensors for real-time tracking of cell growth. *Biotechnology and Bioengineering* **2021**, *118*, 2380–2385.
9. Sander, D. Magnetostriction and magnetoelasticity. *Handbook of Magnetism and Magnetic Materials* **2020**, pp. 1–45.
10. Samourgkanidis, G. Experimental study and characterization of magnetoelastic ribbons as vibration sensors and their application for the identification of cracks in cantilever beams through the dynamic behavior of the beam. PhD thesis, Πανεπιστήμιο Πατρών. Σχολή Πολυτεχνική. Τμήμα Χημικών Μηχανικών. Τομέας ..., 2020.
11. Köster, U.; Herold, U. Crystallization of metallic glasses. *Glassy Metals I: Ionic Structure, Electronic Transport, and Crystallization* **2005**, pp. 225–259.
12. Suryanarayana, C. In situ mechanical crystallization of amorphous alloys. *Journal of Alloys and Compounds* **2023**, *961*, 171032.
13. Grishin, A.M.; Ignakhin, V.; Lugovskaya, L.; Osaulenko, R.; Sekirin, I. Crystallization kinetics and magnetostriction properties of amorphous Fe80-xCoxP14B6 metallic glasses. *Journal of Magnetism and Magnetic Materials* **2020**, *512*, 166972.
14. Wang, W.; Fan, J.; Li, C.; Yu, Y.; Wang, A.; Li, S.; Liu, J. Low-Loss Soft Magnetic Materials and Their Application in Power Conversion: Progress and Perspective. *Energies* **2025**, *18*, 482.
15. Rehalia, V.; Walia, G.; Bhalla, D. Analysing the reduction of no-load losses in distribution transformers on the usage of amorphous alloy. In Proceedings of the AIP Conference Proceedings. AIP Publishing, 2024, Vol. 2900.
16. Sato, A.; Terada, H.; Nagata, T.; Kurita, S.; Matsuda, Y.; Fukui, K.; Azuma, D.; Hasegawa, R. Development of distribution transformer based on new amorphous metals. In Proceedings of the 20th International Conference and Exhibition on Electricity Distribution (CIRED 2009). IET, 2009, p. 0474.
17. Turutin, A.V.; Vidal, J.V.; Kubasov, I.V.; Kislyuk, A.M.; Malinkovich, M.D.; Parkhomenko, Y.N.; Kobeleva, S.P.; Kholkin, A.L.; Sobolev, N.A. Low-frequency magnetic sensing by magnetoelectric metglas/bidomain LiNbO3 long bars. *Journal of Physics D: Applied Physics* **2018**, *51*, 214001.
18. Bichurin, M.; Petrov, R.; Sokolov, O.; Leontiev, V.; Kuts, V.; Kiselev, D.; Wang, Y. Magnetoelectric magnetic field sensors: A review. *Sensors* **2021**, *21*, 6232.
19. Savage, H.; Spano, M. Theory and application of highly magnetoelastic Metglas 2605SC. *Journal of Applied Physics* **1982**, *53*, 8092–8097.
20. Mitchell, E.; DeMoyer, R.; Vranish, J. A new Metglas sensor. *IEEE Transactions on Industrial Electronics* **1986**, pp. 166–170.
21. Jen, S.; Liu, C.; Lin, H.; Chou, S. Frequency dependence of the magnetostrictive phenomenon in Metglas® 2605SA1 ribbon: A minor-loop case. *AIP Advances* **2014**, *4*.
22. Kouzoudis, D.; Baimpos, T.; Samourgkanidis, G. A New Method for the Measurement of the Diffusion Coefficient of Adsorbed Vapors in Thin Zeolite Films, Based on Magnetoelastic Sensors. *Sensors* **2020**, *20*, 3251.
23. Baimpos, T.; Gora, L.; Nikolakis, V.; Kouzoudis, D. Selective detection of hazardous VOCs using zeolite/Metglas composite sensors. *Sensors and Actuators A: Physical* **2012**, *186*, 21–31.
24. Baimpos, T.; Tsukala, V.; Nikolakis, V.; Kouzoudis, D. A modified method for the calculation of the humidity adsorption stresses inside zeolite films using magnetoelastic sensors. *Sensor Letters* **2012**, *10*, 879–885.
25. Samourgkanidis, G.; Nikolaou, P.; Gkovosdis-Louvaris, A.; Sakellis, E.; Blana, I.; Topoglidis, E. Hemin-Modified SnO2/Metglas Electrodes for the Simultaneous Electrochemical and Magnetoelastic Sensing of H2O2. *Coatings* **2018**, *8*, 284.
26. Sagasti, A.; Bouropoulos, N.; Kouzoudis, D.; Panagiotopoulos, A.; Topoglidis, E.; Gutiérrez, J. Nanostructured ZnO in a metglas/ZnO/hemoglobin modified electrode to detect the oxidation of the hemoglobin simultaneously by cyclic voltammetry and magnetoelastic resonance. *Materials* **2017**, *10*, 849.

 doi:10.20944/preprints202505.1546.v1

27. Samourgkanidis, G.; Kouzoudis, D. Magnetoelastic ribbons as vibration sensors for real-time health monitoring of rotating metal beams. *Sensors* **2021**, *21*, 8122.
28. Kouzoudis, D.; Samourgkanidis, G.; Tapeinos, C.I. Contactless Detection of Natural Bending Frequencies using Embedded Metallic-Glass Ribbons inside Plastic Beams made of 3-D Printing. *Recent Progress in Materials* **2021**, *3*, 1–1.
29. Tapeinos, C.I.; Kamitsou, M.D.; Dassios, K.G.; Kouzoudis, D.; Christogerou, A.; Samourgkanidis, G. Contactless and Vibration-Based Damage Detection in Rectangular Cement Beams Using Magnetoelastic Ribbon Sensors. *Sensors* **2023**, *23*, 5453.
30. Samourgkanidis, G.; Kouzoudis, D. A pattern matching identification method of cracks on cantilever beams through their bending modes measured by magnetoelastic sensors. *Theoretical and Applied Fracture Mechanics* **2019**, *103*, 102266.
31. Samourgkanidis, G.; Kouzoudis, D. Experimental detection by magnetoelastic sensors and computational analysis with finite elements, of the bending modes of a cantilever beam with minor damage. *Sensors and Actuators A: Physical* **2018**, *276*, 155–164.
32. Sagasti, A.; Palomares, V.; Porro, J.M.; Orúe, I.; Sánchez-Ilárduya, M.B.; Lopes, A.C.; Gutiérrez, J. Magnetic, magnetoelastic and corrosion resistant properties of (Fe–Ni)-based metallic glasses for structural health monitoring applications. *Materials* **2019**, *13*, 57.
33. Samourgkanidis, G.; Kouzoudis, D. Characterization of magnetoelastic ribbons as vibration sensors based on the measured natural frequencies of a cantilever beam. *Sensors and Actuators A: Physical* **2020**, *301*, 111711.
34. Sarker, P.C.; Islam, M.R.; Guo, Y.; Zhu, J.; Lu, H.Y. State-of-the-art technologies for development of high frequency transformers with advanced magnetic materials. *IEEE Transactions on Applied Superconductivity* **2018**, *29*, 1–11.
35. Mouhamad, M.; Elleau, C.; Mazaleyrat, F.; Guillaume, C.; Jarry, B. Short-circuit withstand tests of metglas 2605SA1-based amorphous distribution transformers. *IEEE transactions on magnetics* **2011**, *47*, 4489–4492.
36. Fang, Z. *Ultra sensitive magnetic sensors integrating the giant magnetoelectric effect with advanced microelectronics*; The Pennsylvania State University, 2011.
37. Kolano, R.; Kolano-Burian, A.; Krykowski, K.; Hetmańczyk, J.; Hreczka, M.; Polak, M.; Szynowski, J. Amorphous soft magnetic core for the stator of the high-speed PMBLDC motor with half-open slots. *IEEE Transactions on Magnetics* **2016**, *52*, 1–5.
38. Austrin, L.; Figueroa-Karlstrom, E.; Engdahl, G. Evaluation of switching losses in magnetic amplifiers as an alternative to IGBT switching technologies. In Proceedings of the 2008 4th IET Conference on Power Electronics, Machines and Drives. IET, 2008, pp. 250–254.
39. Quach, H.P.; Chui, T.C. Low temperature magnetic properties of Metglas 2714A and its potential use as core material for EMI filters. *Cryogenics* **2004**, *44*, 445–449.
40. Luong, V.S.; Le, M.; Quang, V.P. Fluxgate-based displacement sensor design. *Journal of Superconductivity and Novel Magnetism* **2023**, *36*, 1767–1775.
41. Cadogan, J.; Campbell, S.; Jing, J.; Foley, C.; Kater, P.; Mai, Y. Annealing embrittlement of Fe78Si9B13 (METGLAS-2605S2). *Hyperfine Interactions* **2014**, *226*, 7–14.
42. Deng, T.; Chen, Z.; Di, W.; Fang, B.; Luo, H. Enhancement magnetoelectric effect in Metglas-Fe by annealing. *Applied Physics A* **2021**, *127*, 1–11.
43. Lee, D.Y.; Yim, S.H.; Son, D. Effects of Annealing Temperature on Amorphous CoFeCrBSi Alloys for Flux-gate Magnetometers. *Journal of Magnetics* **2021**, *26*, 67–70.
44. Sun, Y.; Zhang, X.; Wu, S.; Zhuang, X.; Yan, B.; Zhu, W.; Dolabdjian, C.; Fang, G. Magnetomechanical properties of Fe-Si-B and Fe-Co-Si-B metallic glasses by various annealing temperatures for actuation applications. *Sensors* **2022**, *23*, 299.
45. Wang, T.; Chen, J.; Wei, R.; Chen, C.; Li, F. Improving the B s and soft magnetic properties of Fe-based amorphous ribbons by manipulating the surface crystallization behavior. *Journal of Materials Science: Materials in Electronics* **2021**, *32*, 21206–21212.
46. Palneedi, H.; Patil, D.R.; Priya, S.; Woo, K.; Ye, J.; Woo, Y.M.; Hwang, Y.S.; Hwang, G.T.; Park, J.H.; Ryu, J. Intense Pulsed Light Thermal Treatment of Pb (Zr, Ti) O3/Metglas Heterostructured Films Resulting in Extreme Magnetoelectric Coupling of over 20 V cm- 1 Oe- 1. *Advanced Materials* **2023**, *35*, 2303553.
47. Samourgkanidis, G.; Varvatsoulis, K.; Kouzoudis, D. The Effect of the Thermal Annealing Process to the Sensing Performance of Magnetoelastic Ribbon Materials. *Sustainability* **2021**, *13*, 13947.
48. Livingston, J.D. Magnetomechanical properties of amorphous metals. *physica status solidi (a)* **1982**, *70*, 591–596.

 doi:10.20944/preprints202505.1546.v1